

Removal of Iron Carbide in Turbulent Flow Conditions and Influence of Iron Carbonate Formation in Aqueous CO₂ Corrosion of Mild Steel

Maria C. Di Bonaventura, * ** *** Bruce Brown, * Marc Singer*

* Institute for Corrosion and Multiphase Technology, Department of Chemical and Biomolecular Engineering, Ohio University, Athens, OH 45701, USA

** Current affiliation: BP America, Houston, TX 77079, USA

***Corresponding author. E-mail address: maria.dibonaventura@bp.com.

ABSTRACT

Iron carbide or cementite (Fe₃C) is often classified as a 'corrosion product' but it is originally found in the materials microstructure and, unlike iron carbonate (FeCO₃), it is not precipitated on the steel surface. Rather, it represents the leftover steel structure once the ferrite phase has been corroded away. Various researchers have found that Fe₃C acts as a diffusion barrier between iron and carbonate ions, which aids in the precipitation of FeCO₃. Previous studies have also considered various material compositions and microstructures favoring FeCO₃ formation. However, the effect of flow has not been considered previously although it plays a critical role in Fe₃C adherence to the steel surface as it is a fragile leftover layer. In this study, a ferritic-pearlitic UNS¹ G10180 material was exposed to flow velocities (0.4, 2 and 6 m/s) and shear stresses (0.8, 20 and 100 Pa) in a thin rectangular flow channel at favorable layer formation conditions (T = 80°C, pH 6.6, initial [Fe²⁺] = 2 ppm, initial S(FeCO₃) ≈ 10). A critical velocity for Fe₃C removal was identified, which further prevented the formation of FeCO₃, although it is fully expected that its value should depend on the operating conditions.

KEY WORDS: Iron carbide, cementite, shear stress, iron carbonate, carbon steel

1 INTRODUCTION

Cementite (Fe₃C) is a metastable compound¹ often classified as a 'corrosion product' although it is found in the material's microstructure. As opposed to iron carbonate (FeCO₃), cementite is not precipitated on the steel surface but appears as a leftover structure once the ferrite phase has partially corroded.

When considering steels with less than 0.76 wt.% C with a ferritic pearlitic microstructure, as shown in Figure 1, the microconstituents are proeutectoid ferrite and pearlite colonies, which are alternating lamellar-like layers of α-ferrite and Fe₃C.^{2,3} Clover, *et al.*,⁴ have demonstrated that corrosion rate depends on material microstructure when the reduction reaction is hydrogen reduction.. It was found that a ferritic-pearlitic microstructure experiences localized corrosion, whereas a tempered martensite or ferritic microstructure undergoes uniform corrosion,⁴ due to preferential corrosion of the ferrite over Fe₃C.

Throughout the literature, it is found that the ferrite phase behaves as an anode relative to the Fe₃C, which acts as a cathode.¹⁻¹¹ Consequently, ferrite corrodes, leaving exposed Fe₃C residues on the surface of the steel.^{8,10,13} The reason for this is because the electric potential of α-ferrite is -0.4 to -0.5 V and the electric potential of Fe₃C is +0.37 V,⁵ with respect to a standard hydrogen electrode at standard conditions. Additionally, the

¹ Unified Numbering System for Metals and Alloys (UNS). UNS numbers are listed in Metals & Alloys in the Unified Numbering System, 10th ed. (Warrendale, PA: SAE International and West Conshohocken, PA: ASTM International, 2004).

ferrite phase tends to progressively corrode at faster rates as the ratio of the cathode to anode surface area becomes larger,⁵ which occurs when the ferrite phase galvanically corrodes over Fe₃C, leaving a large cathode area with respect to the anode surface area.

Various researchers have studied the effect of the Fe₃C layer on the formation of FeCO₃. leamsupapong, *et al.*,¹² found that the presence and nature of Fe₃C plays a governing role with regard to the formation of FeCO₃ on steel when using UNS G10180 ferritic-pearlitic at various pH values. His findings were similar to those of Farelas, *et al.*,¹³ where the authors investigated how an exposed Fe₃C layer affects FeCO₃ formation by testing two dissimilar metals (dissimilar carbon content and microstructure). Both leamsupapong¹² and Farelas¹³ concluded that Fe₃C acts as a diffusion barrier for ferrous ions generated through the corrosion process, increasing the surface Fe²⁺ concentration and pH and favoring the formation of FeCO₃ within the Fe₃C network.

Other authors came to the opposite conclusion and postulated that the exposed Fe₃C, obtained through pre-corrosion of the metal, does not have any effect on the formation of FeCO₃.⁶ However, the authors' observations were due to the fact that most of the Fe₃C had spalled off during the experiment as witnessed by SEM images. When the experimental conditions were set to ensure iron carbonate saturation $S(\text{FeCO}_3)$ values in the range of 300-500, FeCO₃ still formed even after the removal of Fe₃C.

Flow effects are said to play a major role in the formation of FeCO₃ within the pores of Fe₃C since it is weak and fragile,⁵ and thus very susceptible to removal by flowing conditions. Akeer^{14,15} investigated the formation of FeCO₃ at high wall shear stress in a thin rectangular channel used for high velocity single phase flow experiments. Akeer performed experiments for a variety of steel types at highly turbulent conditions ($\tau = 535$ Pa) developed from the beginning of the experiment and found that no protective FeCO₃ layer formed on the surface even at high bulk $S(\text{FeCO}_3)$. Additionally, the high wall shear stress also led to the removal of all iron carbide (Fe₃C) that may have formed.¹⁴

Di Bonaventura tested various steel microstructures under flow velocities equivalent to 0.4 and 0.6 m/s in a 10" pipe with 0.3 and 0.5 Pa wall shear stress, respectively.^{2,3,16} In these studies, it was found that a steel with ferritic-pearlitic microstructure was able to retain the iron carbide layer better than with other microstructures, such as tempered martensite, due to the Fe₃C distribution in the material's microstructure and the higher carbon content (0.18 wt.% C compared to 0.05 wt.% C for tempered martensitic material), which then favored FeCO₃ formation. Within this context, the ferritic-pearlitic microstructure was tested at higher fluid velocities to identify if Fe₃C could be removed due to turbulence and hence impede FeCO₃ formation even at favorable conditions (high $S(\text{FeCO}_3)$).

2 EXPERIMENTAL PROCEDURES

This set of experiments were carried out in equipment built in-house called a Thin Channel Flow Cell (TCFC), which has a 316L stainless steel thin rectangular flow channel (3 mm height, 90 mm width, 600 mm length), shown in Figure 3(a). This test set-up can accommodate up to 4 specimens with a surface area of *ca.* 7cm² (three for surface and cross-section characterization and one for electrochemical measurements). The samples are flush mounted in the flow channel once experimental (including flow regime) conditions have been reached in order avoid oxygen contamination, shown in Figure 3(b). The pH and iron concentration of the solution were not held constant as compared to previous studies;^{2,13} however, due to the large 150-liter (~40 gallon) volume of the TCFC, these parameters, which were monitored continuously, remained relatively stable throughout the course of each experiment. pH was measured with a temperature compensate pH meter and iron concentration tested using a spectrophotometer. This was done by drawing 20 mL out of the TCFC and filtered with 0.45 μm filter; 10 mL were used as a blank solution and

the remaining 10 mL were mixed with an iron reagent. These two solutions were measured against other in order to determine ferrous ion concentration.

Experiments were conducted in a 1 wt.% NaCl electrolyte with initial $S(\text{FeCO}_3) = 10$, achieved by injecting aqueous FeCl_2 (2 grams of $\text{FeCl}_2 \cdot 4\text{H}_2\text{O}$ in 50 mL of deionized water) sparged with nitrogen gas. This saturation value ensured conditions favoring a steady FeCO_3 layer formation. Experiments were conducted at three different water velocities (0.4, 2.0 and 6.0 m/s), enabling comparison with previous studies performed at low velocity,^{3,13,16} and, at the same, enabling determination a critical flow velocity for removal of Fe_3C . The equivalent pipeline velocities in a 10-inch pipe, V_{eq} , assuming the same species mass transfer coefficient, were determined using the Sherwood correlation for a smooth pipe in order to match velocities and shear stresses across various experiments.^{2,3} Wall shear stresses, τ , were determined from correlations and direct measurements using a floating element sensor.^{17,19} The duration of the experiments was five days, enabling sufficient time for Fe_3C to form, as indicated in previous experiments of this kind.^{2,3,12,13,16} The other environmental conditions (pH 6.6, $T = 80^\circ\text{C}$) were selected to ensure optimal corrosion product layer forming conditions, based on the literature review and analyses performed. Experiments at the highest velocity were reproduced in order to determine accuracy of test results. Table 1 summarizes all of the experimental parameters.

2.1 Materials

The UNS G10180 material with a ferritic-pearlitic microstructure was chosen for this set of experiments since this material had shown significant Fe_3C layer/residues of about 40 + 20 mm thickness in previous experiments by XRD and cross-sectional analysis.^{2,3,16} Table 2 provides the composition of the UNS G10180 material. The ferritic pearlitic microstructure is shown in Figure 2 a). Specimens were wet-polished with silicon carbide abrasive paper up to 600 grit in order to ensure uniform preparation, i.e., surface characteristics, prior to the start of experiments; this included rinsing with isopropyl alcohol and use of ultrasonication to remove any residue from the specimen surfaces. Samples were dried with cold air before being mounted.

2.2 Electrochemical Measurements

A Gamry^{II} potentiostat was used for electrochemical measurements. The working electrode was polarized ± 5 mV versus the open circuit potential using a scan rate of 0.125 mV/s for linear polarization resistance (LPR) measurements. Figure 4(a) shows the electrochemical sample used for LPR measurements, where the working electrode (WE) has a surface area of *ca.* 0.88 cm². The counter electrode (CE) is made American Iron and Steel Institute (AISI) 316L stainless steel. The Ag/AgCl reference electrode is located downstream of the test channel. The B value that was used was 26 mV/decade obtained from the literature as being typical for low temperature CO_2 corrosion of mild steel.^{3,5,10,11} The polarization resistance from LPR measurements was used to calculate the current density (i_{corr} , A/cm²) and convert the corrosion rate in millimeters per year (mm/yr) using the Stern-Geary Equation^{1,12,13} as follows:

$$\text{Corrosion rate} \left(\frac{\text{mm}}{\text{yr}} \right) = \frac{\alpha i_{corr} \text{MW}}{\rho n F} \quad (1)$$

Where MW is the molecular weight of iron (g/mol), ρ is the density of iron (g/cm³), n is the number of electrons involved in the electrochemical reaction, F is Faraday's constant, and α is a conversion factor to obtain corrosion rate in mm/yr unit.

Electrochemical impedance spectroscopy (EIS) measurements at high frequencies were obtained in order to gather a solution resistance and correct polarization resistance obtained from LPR measurements.

2.3 Weight Loss and Surface Analysis

Some steel specimens were dismantled on the 3rd and 5th day of the experiments for surface characterization to determine nature of corrosion product present. A JEOL 6390LV^{III} SEM was used to characterize the surface morphology of all specimens and an EDS, coupled to the SEM, was also used for elemental analysis. Raman analysis was also performed using Witec Alpha 300^{IV} Confocal Raman through 20X objective lenses to properly characterize corrosion products. The laser detector was used at a 532 nm wavelength at a laser intensity of ~ 1000 kW/cm². After completion of surface characterization, specimens were mounted in epoxy for cross-sectional analysis of the corrosion product layer using a SEM to characterize the layer morphology, thickness, and surface topography, in order to detect if any formation of FeCO₃ occurred within the Fe₃C network. Weight loss (WL) measurements were also obtained following ASTM G1-03.¹⁷

3 RESULTS AND DISCUSSION

3.1 Water Chemistry

Figure 5 and Figure 6 show changes in water chemistry, pH and ferrous ion concentration, respectively, in the TCFC set up for the UNS G10180 ferritic-pearlitic tested at three different velocities. It can be seen that some deviations from the initial pH and ferrous ion concentration are noticed, due to the fact that these parameters were not controlled as opposed to experiments described in previous studies.^{2,3,14} Changes in water chemistry, especially in pH, can result in saturation value, $S(\text{FeCO}_3)$, deviations. However, these were not drastic as shown in Figure 7, and did not affect the results of this set of experiments, thus, the removal of Fe₃C could be properly analyzed without any environmental factors affecting validity of the results.

3.2 Corrosion Rates

Figure 8 includes both LPR and WL corrosion rate measurements during the course of the experiments with ferritic-pearlitic UNS G10180 tested at three different velocities. It can be seen that for the 0.4 m/s ($V_{eq} = 0.75$ m/s, $\tau = 0.8$ Pa) and 2 m/s ($V_{eq} = 4.7$ m/s, $\tau = 20$ Pa), the corrosion rate increased over time until it reached a value of about 7 mm/yr after about 40 hours. As seen in previous studies, this was because of the progressive exposure of Fe₃C acting as an additional cathodic area and causing galvanic corrosion of the anodic α -ferrite. This stage is commonly described as the active corrosion stage.^{2,3,12,13,16} For the 0.4 m/s ($V_{eq} = 0.75$ m/s, $\tau = 0.8$ Pa), the corrosion rate started decreasing at about the 45th hour to a low and stable value of about 0.2 mm/yr. This can be attributed to the nucleation and growth of FeCO₃.^{2,3,12,13,16} In comparison with results obtained from previous experiments,^{2,3,16} for the same conditions and fluid velocity, there is a good reproducibility of the results even though the experimental set ups were different. For the 2 m/s ($V_{eq} = 4.7$ m/s, $\tau = 20$ Pa) experiments, the corrosion rate started decreasing at about the 60th hour to a low and stable corrosion rate value of about 0.2 mm/yr, similar to the one obtained for 0.4 m/s. For the 6 m/s ($V_{eq} = 12$ m/s, $\tau = 100$ Pa) experiment, however, the corrosion rate was stable at a value of about 4 mm/yr, indicating absence of the active corrosion stage previously observed at the lower velocities. This stable corrosion rate value is attributed to the removal of Fe₃C, which caused the corrosion rate behavior to perform similarly to that of pure iron, as seen in previous studies.² The high and stable corrosion rate also correlates well with Akeer's previous findings.¹⁴ Additionally, the time averaged weight loss corrosion rates show a similar trend: for the 6 m/s ($V_{eq} = 12$ m/s, $\tau =$

100 Pa) experiment, the corrosion rate was 9.4 mm/yr, which was significantly higher than the two other measurements at lower velocities. Lastly, the corrosion rate obtained through weight loss measurements does not match the corrosion rate obtained through electrochemical measurements, which is similar to the findings in UNS G10180 ferritic-pearlitic since the presence of Fe₃C accelerates electrochemical corrosion rates.

LPR corrosion rate results shown in Figure 8 obtained from the TCFC experiments were compared with those obtained with a 4-liter, controlled mass transfer and controlled water chemistry setup described in previous studies.^{2,3,16} In the previous studies performed in a 4-liter glass cell, FeCO₃ formed after *ca.* 100 hours at 250 rpm ($Ve_{eq} = 0.6$ m/s, $\tau = 0.5$ Pa). In comparison, FeCO₃ formation in the TCFC at 0.4 m/s ($Ve_{eq} = 0.75$ m/s, $\tau = 0.8$ Pa) occurred after *ca.* 40 hours, which both showed that minor to no precipitation of FeCO₃ occurred.

3.3 Surface Morphologies and Characterization

Figure 9 shows the surface morphologies of the specimens taken out on days 3 and 5 for each experiment. For the 0.4 m/s ($Ve_{eq} = 0.75$ m/s, $\tau = 0.8$ Pa) and 2 m/s ($Ve_{eq} = 4.7$ m/s, $\tau = 20$ Pa) experiments, specimens for days 3 and 5 show similar surface morphologies with a non-uniform surface. This uneven surface confirms that the preferential dissolution of ferrite had occurred, while the Fe₃C acted as a cathode and remained on the steel surface.^{1, 5-8,10,11,14} The 0.4 m/s specimen surface morphology is similar to the findings from previous studies under the same environmental conditions,^{2,3,16} as FeCO₃ prisms precipitated on the surface of the specimens. The 2 m/s ($Ve_{eq} = 4.7$ m/s, $\tau = 20$ Pa) specimens also show some FeCO₃ precipitation on the steel surface. Raman spectra shown in Figure 10 and Figure 11 for 0.4 m/s ($Ve_{eq} = 0.75$ m/s, $\tau = 0.8$ Pa) and 2 m/s ($Ve_{eq} = 4.7$ m/s, $\tau = 20$ Pa) specimens, respectively, retrieved after day 5, confirm that the corrosion product was FeCO₃ based on spectra obtained from the literature.²⁰⁻²²

For the 6 m/s ($Ve_{eq} = 12$ m/s, $\tau = 100$ Pa) specimen, however, a bare steel surface with small, disconnected residues is observed, which may be due to the almost complete removal of Fe₃C due to turbulent conditions. There was no evidence of initial polishing marks or grooves, which can be indicative of carbide remaining on the steel surface.^{12,13} This surface morphology shows similar results to Akeer's previous study.¹⁴ Figure 12 (a) shows SEM images of locations used for EDS analysis in order to determine the nature of the residues; the points labeled 1 and 2 were analyzed. Figure 12 (b) shows the EDS spectrum for the point labeled 1 which analyzes the residue. It is noteworthy that there was enrichment of alloying elements (87 atom% Fe, 5.4 atom% Cu, 3.3 atom% Ni, 2.4 atom% Mn and 1.9 atom% Cr) and as indicated by the atom% values, there was no significant presence of carbon. Given the appearance of the specimen surface and surface enrichment with respect to the alloying elements of the UNS G10180, this was not indicative of Fe₃C remaining on the surface as witnessed in previous studies.³ EDS analysis was also performed on the point labeled 2 on Figure 12 (a), which showed that this is indeed a bare steel surface as only the presence of iron was detected. This finding correlates with Akeer's previous study, where no carbide was witnessed on the surface of such a steel specimen exposed to high flow velocity.¹⁴

Raman analysis was also performed to determine if there was evidence of any corrosion product on the surface of the specimen, shown in Figure 13. It can be seen that there was no peak corresponding to siderite (1084 cm⁻¹). However, a peak was found at 693 cm⁻¹. Upon searching of the literature on Raman spectroscopy and given the content of alloying elements in the UNS G10180, shown in Table 2, it was found that this peak could correspond to FeCr₂O₄ (chromite).²³ Raman spectra, surface morphologies, EDS analysis and corrosion rate trend obtained from LPR measurements confirm that no FeCO₃ formed on the specimen surface and no Fe₃C was retained. Fe₃C was removed by high flow velocities, similar to what Akeer established.¹⁴

3.4 Cross-Sectional Morphologies

Figure 14 shows cross-sectional morphologies of specimens shown in Figure 9. The 0.4 m/s ($Ve_{eq} = 0.75$ m/s, $\tau = 0.8$ Pa) specimens show a Fe_3C network with $FeCO_3$ precipitation, which correlates to the corrosion rate shown in Figure 8. These results are similar to what was found in the same test conditions in previous studies.^{2,3,16} The 2 m/s ($Ve_{eq} = 4.7$ m/s, $\tau = 20$ Pa) specimen also shows a Fe_3C network with $FeCO_3$ precipitation. However, the Fe_3C network is more visible in areas where precipitation of $FeCO_3$ did not occur. On the other hand, the 6 m/s ($Ve_{eq} = 12$ m/s, $\tau = 100$ Pa) specimen shows no significant Fe_3C network nor $FeCO_3$ precipitation, which can further confirm that the removal of Fe_3C occurred and hence prevented the precipitation of $FeCO_3$. This is also supported by the corrosion rate trend shown in Figure 9, for the 6 m/s ($Ve_{eq} = 12$ m/s, $\tau = 100$ Pa) experiment, where the corrosion rate was high and stable over time.¹²⁻¹⁴

4 CONCLUSIONS

The TCFC (a corrosion testing system with very controlled flow conditions) was used to identify the velocity required for removal of a Fe_3C layer, considering a steel with ferritic-pearlitic microstructure. At the lowest velocity tested ($Ve_{eq} = 0.75$ m/s, $\tau = 0.8$ Pa), similar results were obtained as in previous studies where $FeCO_3$ precipitation within Fe_3C network occurred and caused a decrease in the corrosion rate. At the highest velocity tested ($Ve_{eq} = 12$ m/s, $\tau = 100$ Pa), $FeCO_3$ did not precipitate due to removal of Fe_3C layer even though water chemistry was favorable at $S(FeCO_3) \approx 10$. These results indicate that flow can impact surface precipitation of $FeCO_3$ due to the removal of Fe_3C from the steel surface.

5 ACKNOWLEDGMENTS

Authors would like to thank sponsors of the Corrosion Center Joint Industry Project at the Institute for Corrosion and Multiphase Technology for their financial support (Anadarko, Baker Hughes, BP, Chevron, China National Offshore Oil Corporation, ConocoPhillips, DNV GL, ExxonMobil, M-I SWACO, Occidental Oil Company, Petroleum Institute, PTT, Saudi Aramco, Shell Global Solutions, SINOPEC, TOTAL, TransCanada, & WGK), Ali Raifei and Prof. Hugh Richardson at the Ohio University Department of Chemistry and Biochemistry for usage of analytical equipment, as well as Alexis Barxias and Cody Shafer for their assistance in the laboratory.

6 REFERENCES

1. W.D. Callister, D.G. Rethwisch, *Materials Science and Engineering: An Introduction*, 9th ed. (New York, NY: Wiley, 2007), p.665-715.
2. M. Di Bonaventura, *Effect of Flow on the Formation of Iron Carbonate and Influence of Exposed Iron Carbide Layer*. (Master's thesis, Ohio University, 2017)
3. M. Di Bonaventura, B. Brown, S. Nestic, M. Singer, *Effect of Flow and Steel Microstructure on the Formation of Iron Carbonate*, *Corrosion* 75, 10 (2019): p. 1183-1193.
4. D. Clover, B. Kinsella, B. Pejicic, R. De Marco, *The Influence of Microstructure on the Corrosion Rate of Various Carbon Steels*, *Journal of Applied Electrochemistry* 35, 2 (2005): p. 139-149.
5. A. Groysman, *Corrosion for Everybody* (Springer Science & Business Media, 2009), p. 21-29
6. T. Berntsen, M. Seiersten, T. Hemmingsen, *Effect of $FeCO_3$ Supersaturation and Carbide Exposure on the CO_2 Corrosion Rate of Carbon Steel*, *Corrosion* 69, 6 (2013): p.601-613.

7. D.N. Staicopolus, The Role of Cementite in the Acidic Corrosion of Steel, *Journal of the Electrochemical Society* 110, 11 (1963): p.121-1124.
8. F.F. Eliyan, A. Alfantazi, On the Theory of CO₂ Corrosion Reactions – Investigating their Interrelation with the Corrosion Products and API-X100 Steel Microstructure, *Corrosion Science* 85 (2014): p.380-393.
9. S. Al-Hassan, B. Mishra, D.L. Olson, M.M. Salama, Effect of Microstructure on Corrosion of Steels in Aqueous Solutions Containing Carbon Dioxide, *Corrosion* 54, 6 (1998): p.480-491.
10. J.L. Crolet, N. Thevenot, S. Nestic, Role of Conductive Corrosion Products in the Protectiveness of Corrosion Layers, *Corrosion* 54, 3 (1998): p. 194-203.
11. W. Farida, T. Hemmingsen, T. Berntsen, P. Rabindran, Effect of Precorrosion and Temperature on the Formation Rate of Iron Carbonate Film, 7th Pipeline Technology Conference, p.1-16 (2012).
12. S. Imsupapong, B. Brown, M. Singer, S. Nestic, Effect of Solution pH on Corrosion Product Layer Formation in a Controlled Water Chemistry System, *CORROSION/2017*, paper no. 9160 (Houston, TX: NACE, 2017).
13. F. Farelas, B. Brown, S. Nestic, Iron Carbide and its Influence on the Formation of Protective Iron Carbonate in CO₂ Corrosion of Mild Steel, *CORROSION/2013*, paper no. 2291 (Houston, TX: NACE, 2013).
14. E. S. Akeer, Effect of Carbon Steel Composition and Microstructure on CO₂ Corrosion. (PhD Dissertation, Ohio University, 2014)
15. E. Akeer, B. Brown, S. Nestic, The Influence of Mild Steel Metallurgy on the Initiation of Localized CO₂ Corrosion in Flowing Conditions, *CORROSION/2013*, paper no. 2383 (Houston, TX: NACE, 2013).
16. M. Di Bonaventura, B. Brown, S. Nestic, M. Singer, Effect of Flow and Steel Microstructure on the Formation of Iron Carbonate, *CORROSION/2018*, paper no. 11179 (Houston, TX: NACE, 2018).
17. ASTM G1-03, “Standard Practice for Preparing, Cleaning, and Evaluating Corrosion Test Specimens” (West Conshohocken, PA: ASTM International, 2011)
18. W. Li, Y. Xiong, B. Brown, K. Kee, S. Nestic, Measurement of Wall Shear Stress in Multiphase Flow and its Effect on Protective FeCO₃ Corrosion Product Layer Removal, *CORROSION/2015*, paper no. 5922 (Houston, TX: NACE 2015).
19. C. Patel. M. R. Head, Some Observations on Skin Friction and Velocity Profiles in Fully Developed Pipe and Channel Flows, *Journal of Fluid Mechanics* 38, 01 (1969) p. 181-201.
20. Azoulay, E. Conforto, P. Refait, C. Remazeilles, Study of Ferrous Corrosion Products on Iron Archaeological Objects by Electron Backscattered Diffraction (EBSD), *Applied Physics A*, 110, 2 (2013): p. 379-388.
21. S. J. Oh, D. C. Cook, H. E. Townsend, Characterization of Iron Oxides Commonly Formed as Corrosion Products on Steel, *Hyperfine Interactions*, 112, 1-4 (1998): p.59-66.
22. Remazeilles, A. Dheilly, S. Sable, I. Lanneluc, D. Neff, P. Refait, Microbiologically Induced Corrosion Process of Archaeological Iron Nails from the Sixteenth Century, *Corrosion Engineering Science and Technology*, 45, 5 (2010): p. 388-394.
23. Wang, K. E. Kuebler, B. L. Jolliff, L. A. Haskin, Raman Spectroscopy of Fe-Ti-Cr-Oxides, Case Study: Marian Meteorite EETA79001, *American Mineralogist* 89, 5-6 (2004): p. 665-680.

7 FIGURE CAPTIONS

Figure 1. SEM image of ferritic-pearlitic microstructure of UNS G10180^{2,3}

Figure 2. (a) Thin Channel Flow Cell (TCFC) (b) specimen mount and flow test section of TCFC (images courtesy of Cody Shafer, ICMT)

Figure 3. Specimens used for TCFC experiments (a) electrochemical specimen (b) characterization specimens¹³

Figure 4. Comparison of pH over time for 0.4 m/s ($V_{eq} = 0.75$ m/s, $\tau = 0.8$ Pa), 2 m/s ($V_{eq} = 4.7$ m/s, $\tau = 20$ Pa) and 6 m/s ($V_{eq} = 12$ m/s, $\tau = 100$ Pa) experiments with ferritic-pearlitic UNS G10180

Figure 5. Comparison of [Fe²⁺] over time for 0.4 m/s ($V_{eq} = 0.75$ m/s, $\tau = 0.8$ Pa), 2 m/s ($V_{eq} = 4.7$ m/s, $\tau = 20$ Pa) and 6 m/s ($V_{eq} = 12$ m/s, $\tau = 100$ Pa) experiments with ferritic-pearlitic UNS G10180

Figure 6. Comparison of $S(\text{FeCO}_3)$ over time for 0.4 m/s ($V_{eq} = 0.75$ m/s, $\tau = 0.8$ Pa), 2 m/s ($V_{eq} = 4.7$ m/s, $\tau = 20$ Pa) and 6 m/s ($V_{eq} = 12$ m/s, $\tau = 100$ Pa) experiments with ferritic-pearlitic UNS G10180

Figure 7. Comparison of LPR corrosion rate over time for 0.4 m/s ($V_{eq} = 0.75$ m/s, $\tau = 0.8$ Pa), 2 m/s ($V_{eq} = 4.7$ m/s, $\tau = 20$ Pa) and 6 m/s ($V_{eq} = 12$ m/s, $\tau = 100$ Pa) experiments with ferritic-pearlitic UNS G10180. Legend highlights the weight loss (wl) measurements at the end of the experiment

Figure 8. SEM images showing comparison of surface morphologies over time for 0.4 m/s ($V_{eq} = 0.75$ m/s, $\tau = 0.8$ Pa), 2 m/s ($V_{eq} = 4.7$ m/s, $\tau = 20$ Pa) and 6 m/s ($V_{eq} = 12$ m/s, $\tau = 100$ Pa) experiments with ferritic-pearlitic UNS G10180

Figure 9. Raman spectra of surface confirming FeCO_3 as a corrosion product for 0.4 m/s ($V_{eq} = 0.75$ m/s, $\tau = 0.8$ Pa) experiment with ferritic-pearlitic UNS G10180

Figure 10. Raman spectra of surface confirming FeCO_3 as a corrosion product for 2 m/s ($V_{eq} = 4.7$ m/s, $\tau = 20$ Pa) experiment with ferritic-pearlitic UNS G10180

Figure 11. (a) SEM image used for EDS analysis showing surface morphology after day 5 for 6 m/s ($V_{eq} = 12$ m/s, $\tau = 100$ Pa) experiment with ferritic-pearlitic UNS G10180, (b) EDS spectrum taken at point labeled 1 in (a) confirming presence of alloying elements

Figure 12. Raman spectra of surface for 6 m/s ($V_{eq} = 12$ m/s, $\tau = 100$ Pa) experiment with ferritic-pearlitic UNS G10180

Figure 13. SEM images showing cross-sectional morphologies over time for 0.4 m/s ($V_{eq} = 0.75$ m/s, $\tau = 0.8$ Pa), 2 m/s ($V_{eq} = 4.7$ m/s, $\tau = 20$ Pa) and 6 m/s ($V_{eq} = 12$ m/s, $\tau = 100$ Pa) experiments with ferritic-pearlitic UNS G10180

8 TABLES

Table 1. Test matrix showing experimental parameters used to study the removal of Fe_3C

Parameters	Conditions
Experimental Setup	Thin Channel Flow Cell (TCFC)
Materials (microstructure)	UNS G10180 (ferrite-pearlite)
Electrolyte	1 wt.% NaCl aqueous solution
Total Pressure	1 bar (10^5 Pa)
Temperature	80°C
CO ₂ Partial Pressure	0.53 bar (5.3×10^4 Pa)
pH	6.6 ± 0.03
Initial $[\text{Fe}^{2+}]$	2 ± 1 ppm
Saturation w.r.t. FeCO_3	10 – 30
Flow Velocity	0.4, 2.0 and 6.0 m/s
Equivalent Pipeline Velocity in 10" pipe, $V_{eq}^{2,3}$	0.75, 4.7, and 12.0 m/s
Shear Stress, τ	0.8, 20, and 100 Pa
Surface Analysis	SEM, Raman, and Cross-Section
Corrosion Measurement Methods	OCP, LPR, EIS and weight loss

Table 2. Chemical composition of UNS G10180 (wt.%)

UNS G10180 (balance Fe)									
Al	As	C	Co	Cr	Cu	Mn	Mo	Nb	Ni
0.008	0.006	0.18	0.003	0.12	0.18	0.75	0.020	0.002	0.065
P	S	Sb	Si	Sn	Ti	V	W	Zn	Zr
0.011	0.021	0.009	0.16	0.009	0.002	0.003	0.014	0.004	0.003

8.1.1 Figures

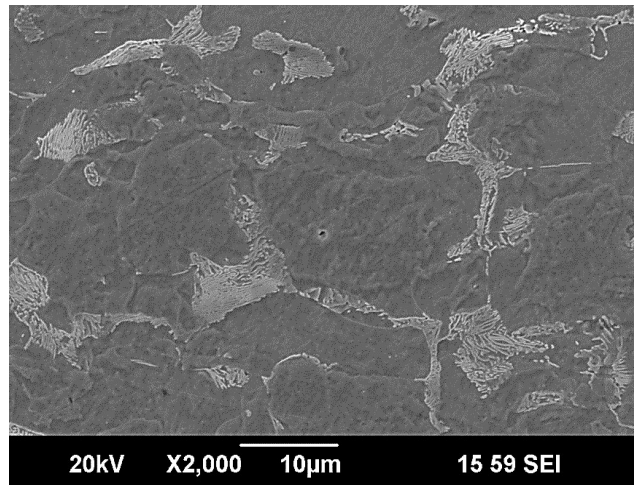
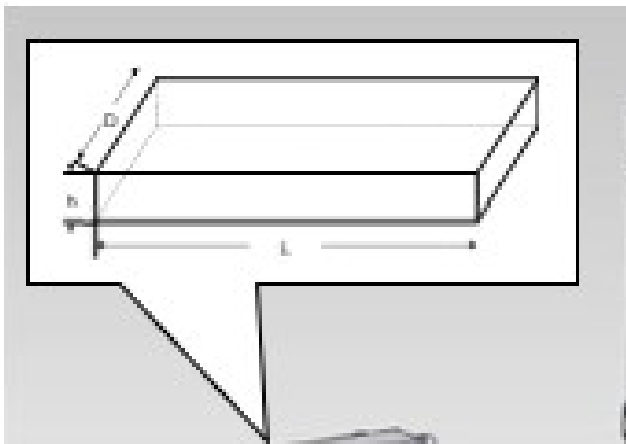


Figure 2. SEM image of ferritic-pearlitic microstructure of UNS G10180^{2,3}



(a)



(b)

Figure 3. (a) Thin Channel Flow Cell (TCFC) (b) specimen mount and flow test section of TCFC (images courtesy of Cody Shafer, ICMT)



Figure 4. Specimens used for TCFC experiments (a) electrochemical specimen (b) characterization specimens¹³

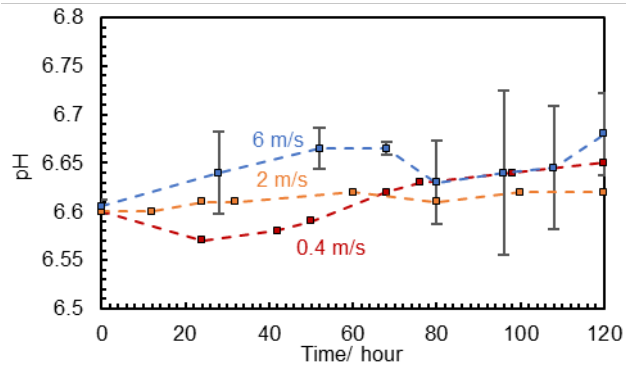


Figure 5. Comparison of pH over time for 0.4 m/s ($V_{eq} = 0.75$ m/s, $\tau = 0.8$ Pa), 2 m/s ($V_{eq} = 4.7$ m/s, $\tau = 20$ Pa) and 6 m/s ($V_{eq} = 12$ m/s, $\tau = 100$ Pa) experiments with ferritic-pearlitic UNS G10180

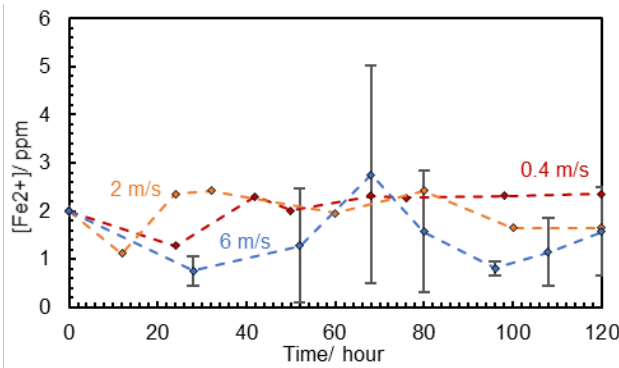


Figure 6. Comparison of $[Fe^{2+}]$ over time for 0.4 m/s ($V_{eq} = 0.75$ m/s, $\tau = 0.8$ Pa), 2 m/s ($V_{eq} = 4.7$ m/s, $\tau = 20$ Pa) and 6 m/s ($V_{eq} = 12$ m/s, $\tau = 100$ Pa) experiments with ferritic-pearlitic UNS G10180

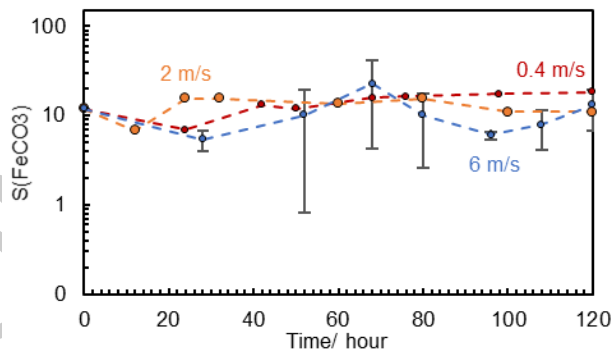


Figure 7. Comparison of $S(FeCO_3)$ over time for 0.4 m/s ($V_{eq} = 0.75$ m/s, $\tau = 0.8$ Pa), 2 m/s ($V_{eq} = 4.7$ m/s, $\tau = 20$ Pa) and 6 m/s ($V_{eq} = 12$ m/s, $\tau = 100$ Pa) experiments with ferritic-pearlitic UNS G10180

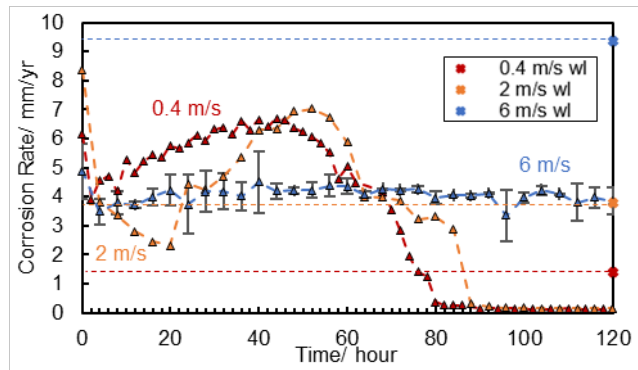


Figure 8. Comparison of LPR corrosion rate over time for 0.4 m/s ($V_{eq} = 0.75$ m/s, $\tau = 0.8$ Pa), 2 m/s ($V_{eq} = 4.7$ m/s, $\tau = 20$ Pa) and 6 m/s ($V_{eq} = 12$ m/s, $\tau = 100$ Pa) experiments with ferritic-pearlitic UNS G10180. Legend highlights the weight loss (wl) measurements at the end of the experiment

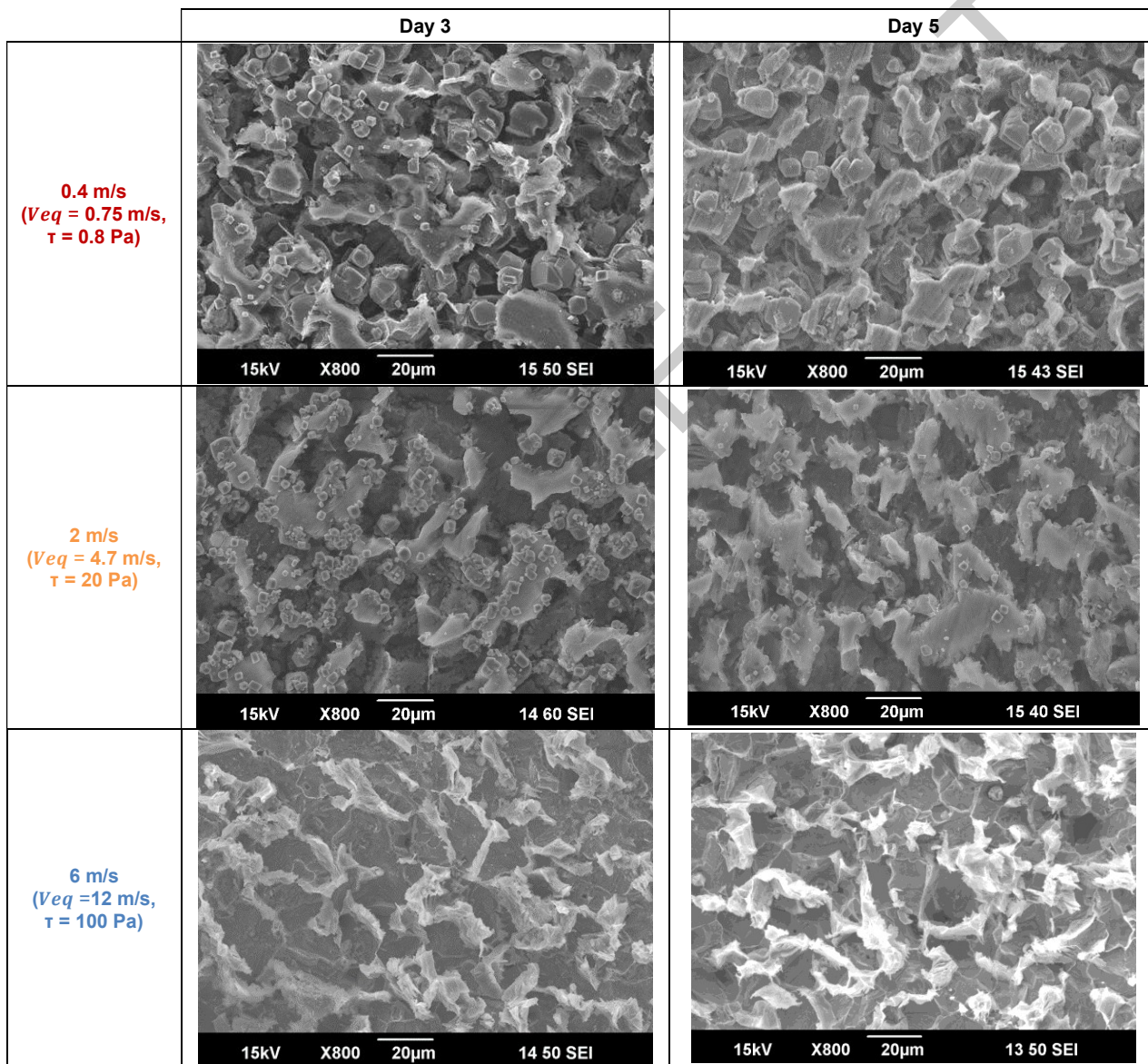


Figure 9. SEM images showing comparison of surface morphologies over time for 0.4 m/s ($V_{eq} = 0.75$ m/s, $\tau = 0.8$ Pa), 2 m/s ($V_{eq} = 4.7$ m/s, $\tau = 20$ Pa) and 6 m/s ($V_{eq} = 12$ m/s, $\tau = 100$ Pa) experiments with ferritic-pearlitic UNS G10180

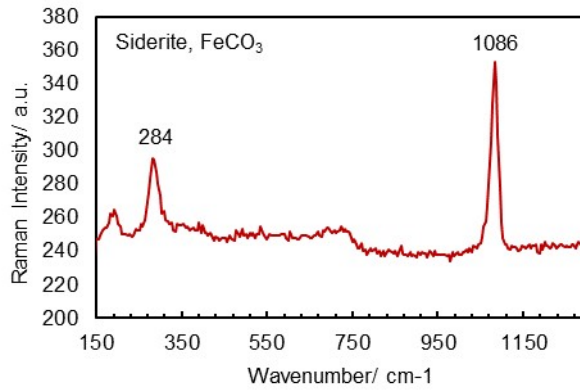


Figure 10. Raman spectra of surface confirming FeCO₃ as a corrosion product for 0.4 m/s ($V_{eq} = 0.75$ m/s, $\tau = 0.8$ Pa) experiment with ferritic-pearlitic UNS G10180

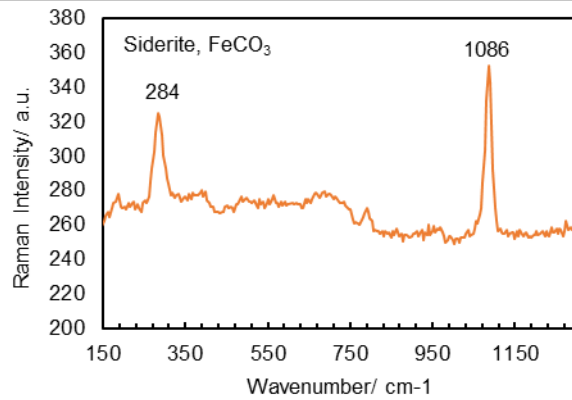


Figure 11. Raman spectra of surface confirming FeCO₃ as a corrosion product for 2 m/s ($V_{eq} = 4.7$ m/s, $\tau = 20$ Pa) experiment with ferritic-pearlitic UNS G10180

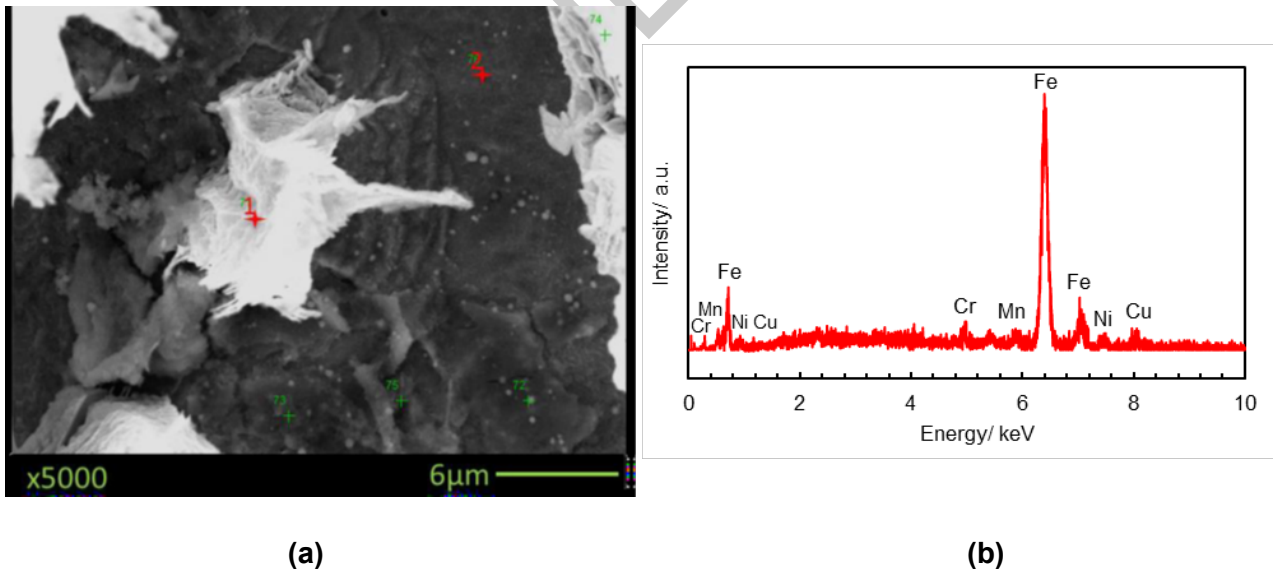


Figure 12. (a) SEM image used for EDS analysis showing surface morphology after day 5 for 6 m/s ($V_{eq} = 12$ m/s, $\tau = 100$ Pa) experiment with ferritic-pearlitic UNS G10180, (b) EDS spectrum taken at point labeled 1 in (a) confirming presence of alloying elements

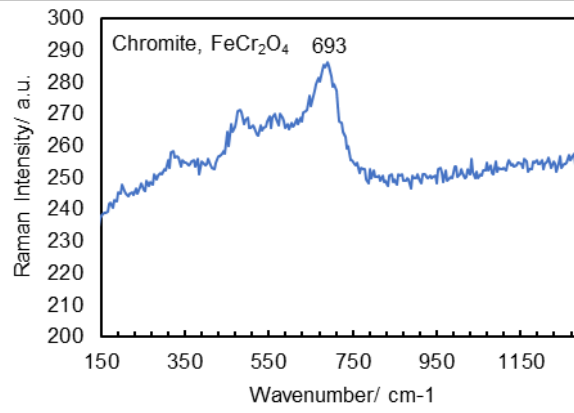


Figure 13. Raman spectra of surface for 6 m/s ($V_{eq} = 12$ m/s, $\tau = 100$ Pa) experiment with ferritic-pearlitic UNS G10180

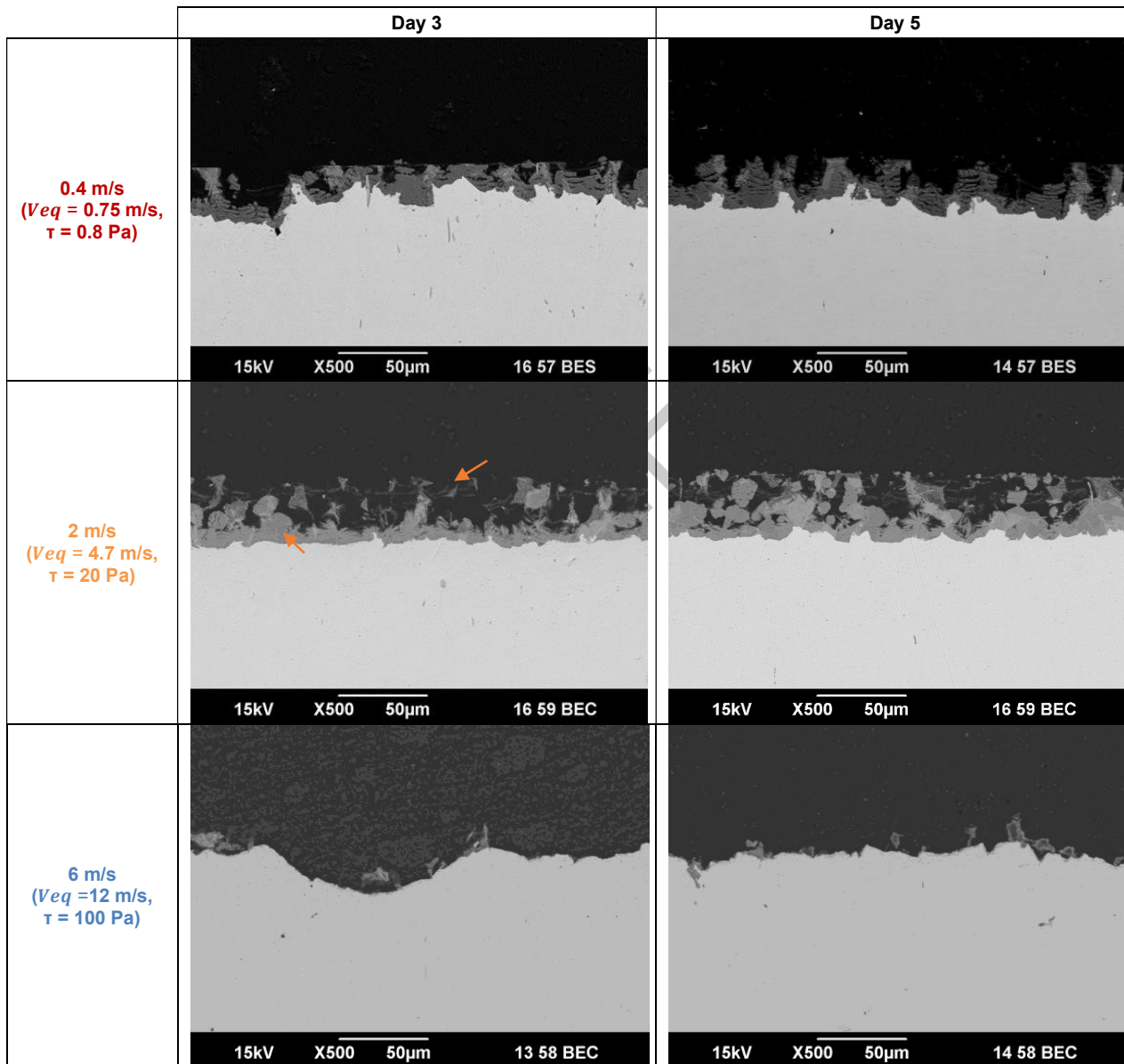


Figure 14. SEM images showing cross-sectional morphologies over time for 0.4 m/s ($V_{eq} = 0.75$ m/s, $\tau = 0.8$ Pa), 2 m/s ($V_{eq} = 4.7$ m/s, $\tau = 20$ Pa) and 6 m/s ($V_{eq} = 12$ m/s, $\tau = 100$ Pa) experiments with ferritic-pearlitic UNS G10180